Modified phase-field-based lattice Boltzmann model for incompressible multiphase flows

Xingchun Xu,[1] Yanwei Hu,[2] Bing Dai,[1] Lei Yang,[1] Jiecai Han,[1] Yurong He,[2] and Jiaqi Zhu[1,3,*]
[1]*National Key Laboratory of Science and Technology on Advanced Composites in Special Environments, Harbin Institute of Technology, Harbin 150080, China*
[2]*School of Energy Science & Engineering, Harbin Institute of Technology, Harbin 150001, China*
[3]*Key Laboratory of Micro-systems and Micro-structures Manufacturing, Ministry of Education, Harbin 150080, China*

(Received 30 April 2020; revised 13 January 2021; accepted 2 September 2021; published 17 September 2021)

Based on the phase-field theory, a multiple-relaxation-time (MRT) lattice Boltzmann model is proposed for the immiscible multiphase fluids. In this model, the local Allen-Chan equation is chosen as the target equation to capture the phase interface. Unlike previous MRT schemes, an off-diagonal relaxation matrix is adopted in the present model so that the target phase-field equation can be recovered exactly without any artificial terms. To check the necessity of removing those artificial terms, comparative studies were carried out among different MRT schemes with or without correction. Results show that the artificial terms can be neglected at low March number but will cause unphysical diffusion or interface undulation instability for the relatively large March number cases. The present modified model shows superiority in reducing numerical errors by adjusting the free parameters. As the interface transport coupled to the fluid flow, a pressure-evolution lattice Boltzmann equation is adopted for hydrodynamic properties. Several benchmark cases for multiphase flow were conducted to test the validity of the present model, including the static drop test, Rayleigh-Taylor instability, and single rising bubble test. For the rising bubble simulation at high density ratios, bubble dynamics obtained by the present modified MRT lattice Boltzmann model agree well with those obtained by the FEM-based level set and FEM-based phase-field models.

DOI: 10.1103/PhysRevE.104.035305

I. INTRODUCTION

Multiphase flows have long been subject to significant interest in both science and engineering [1]. From the computational point of view, it is always the focus and difficulty to capture the phase interface in an accurate, physically consistent, and cost-effective way. The front-capturing approach has long been widely applied to simulate such moving-interface problems. In such approach, only the fixed grids are adopted and no explicit information about the phase interface is required. The interface motion can be obtained by solving the phase indicator function over the whole domain, which makes it relatively easy to implement. Typical front-capturing methods include the volume-of-fluid (VOF), level-set [2], phase-field [3], and hybrid methods related, such as level set coupled with VOF [4] and phase-field coupled with VOF [5].

As a diffuse-interface method, the phase-field method has emerged as one of the most promising approaches for modeling multiphase flows because of its physical origins, simplicity, and scalability. In this method, an order parameter is introduced to describe the phase transition, which has constant values in the bulk phases and varies smoothly across the diffused interface in a hyperbolic tangent or similar fashion. Traditionally, the dynamical evolution for the order parameter is given by the Cahn-Hilliard equation (CHE) [6,7] or Allen-Cahn equation (ACE) [8]. The former is a more popular option for multiphase flow as it takes on a flux-conservative form. Unfortunately, although the order parameter in CHE is conserved globally, spontaneous shrinkage (mass leakage) of drops or bubbles is inherent to such method [9]. In order to minimize the shrinkage effect, the profile-corrected [10] and flux-corrected [11] formulations were developed by adding flux terms. The fourth-order spatial derivative in original CHE and additional flux terms in modified versions make these equations very cumbersome to solve. The Allen-Cahn equation is easier to handle numerically due to the fact that only second-order derivative terms are needed to be discretized. Many efforts have been made to improve its mass conservation. Sun and Beckermann [12] developed a modified ACE by subtracting out the curvature-driven interface motion. Later, inspired by the conservative level-set method [13], Chiu and Lin [14] reformulated this equation in a conservative form, referred to as local ACE here. Another kind of conservative ACE was proposed through introducing a Lagrange multiplier [15,16], which is called the nonlocal ACE.

Rooted in kinetic theory, the lattice Boltzmann (LB) method has attracted considerable attention in modeling multiphase fluid systems. The existing multiphase LB models include color-gradient model [17], pseudopotential model [18–21], free-energy model [22], kinetic model [23,24], and phase-field-based model [25–32]. A comprehensive overview of different multiphase LB models can be found in Refs. [33,34]. Here we only focus on the phase-field-based LB models. The double-distribution-function approach is applied for this kind of model, in which one distribution function is

---

[*] zhujq@hit.edu.cn

adopted for the fluid flow and the other is for interface capturing. Although several LB schemes have been proposed for above-mentioned CHE and ACE, there exists a deviation term in the recovered macroscopic equation through the Chapman-Enskog analysis. To overcome such deficiency, Zheng *et al.* [25] introduced a spatial difference term of the distribution equation in the LB equation to remove such deviation term in the recovered CHE. Later, Zu and He [26] applied similar strategy by introducing a spacial difference term of the equilibrium state instead. We note that both modified models for CHE cannot be conducted locally in the collision process, which weakens the advantages of parallel computing in LB method. Another possible way to eliminate the deviation term is to add a source term in the evolution equation [35,36]. Liang *et al.* [28] proposed a modified LB model for Cahn-Hilliard equation by adding a temporal derivative of phase-field flux. Later, based on the fourth-order Chapman-Enskog expansion, Zhang *et al.* [37] developed a high-order LB model for the same target equation to improve the accuracy and stability. With the inclusion of correction terms, the modified model is able to recover the CHE up to third order. As for the Allen-Cahn equation, relatively fewer works based on the framework of LB method have been reported. Geier *et al.* [31] first proposed a LB model for the local ACE, which shows higher accuracy than the CHE-based model. Later, they extended their model to the three-dimensional case [38,39] and ternary fluids [40]. Note that their LB models for ACE have a common defect. They adopted the nonlinear equilibrium but did nothing to eliminate the deviation terms, which may cause numerical errors for the case with relatively large Mach number. Following the strategy to recover the correct CHE in Ref. [28], both the SRT and MRT schemes to remove the additional term in local ACE were developed in Refs. [30,32]. A comparative study between the improved MRT model and the Geier's SRT model was conducted by Ren *et al.* [32]. However, although the deviation term has been removed, we did not find any obvious improvements on numerical accuracy in their benchmark tests. The necessity to remove the deviation term needs to be illustrated in more stringent conditions.

Recently, Huang and Wu [41] proposed a modified MRT LB model to recover the convection-diffusion equation with anisotropic diffusion coefficients. Inspired from their model as well as Refs. [25,26], here we proposed an alternative MRT lattice Boltzmann model for the local Allen-Cahn equation. By introducing an off-diagonal relaxation matrix, the moment vectors are coupled, which is used to produce diffusion effects so that the correct macroscopic equation can be recovered. Free parameters in equilibrium moment vectors and relaxation matrix are adjusted to improve the numerical accuracy and stability. Different from previous models, no spatial or temporal difference terms are introduced here to remove the deviation terms, which makes it easy to implement the algorithm on parallel machines. It should be pointed out that the present modified model can be easily extended to solve the nonlocal Allen-Cahn equation and the Cahn-Hillard equation.

The rest of this paper is organized as follows. In Sec. II, we introduce the phase-field theory and then present the newly developed MRT lattice Boltzmann model for multiphase fluid systems. A variety of Benchmark tests are conducted in Sec. III and Sec. IV, followed by summaries in Sec. V.

II. METHODOLOGY

A. Conservative local ACE

In the phase-field theory, a binary fluid can be described by an order parameter field $\phi(\boldsymbol{r}, t)$, where $\boldsymbol{r}$ denotes the spatial coordinates while t is time. The free-energy functional of such system can be simply presented in the Ginzburg-Landau form [42]

$$\mathcal{F}[\phi] = \int_{\Omega} \left\{ \psi(\phi) + \frac{\varepsilon_{\phi}^{2}}{2} [\nabla \phi]^{2} \right\} d\boldsymbol{r}, \tag{1}$$

where the term $\psi(\phi)$ is a double-well potential to describe the bulk free-energy density, and the square gradient is the gradient energy. A simple prescription for $\psi(\phi)$ is chosen as [28]

$$\psi(\phi) = \beta(\phi - \phi_l)^2(\phi - \phi_h)^2, \tag{2}$$

which determines the values of ϕ in buck phases ($\phi_h > \phi_l$) such that the interface location is given by $(\phi_l + \phi_h)/2$. Coefficients ε_ϕ and β are related to the surface tension σ and interface width W by [32]

$$\varepsilon_{\phi}^{2} = \frac{3}{2|\phi_h - \phi_l|^2} W\sigma \tag{3}$$

and

$$\beta = \frac{12\sigma}{|\phi_h - \phi_l|^4 W}. \tag{4}$$

By minimizing the free energy in Eq. (1), one can obtain the phase field profile for the flat interface at equilibrium state along the z-axis direction normal to the interface,

$$\phi(z) = \frac{\phi_h + \phi_l}{2} + \frac{\phi_h - \phi_l}{2} \tanh\left(\frac{2z}{W}\right). \tag{5}$$

The dynamical evolution for the order parameter is governed by the Allen-Cahn equation [42]

$$\partial_t \phi + \boldsymbol{u} \cdot \nabla \phi = M_{\phi} \left(\nabla^2 \phi - \frac{1}{\varepsilon_{\phi}^{2}} \frac{d\psi}{d\phi} \right), \tag{6}$$

where M_ϕ is the mobility coefficient and $\boldsymbol{u}$ is the macroscopic velocity vector. Equation (6) describes the dynamics of a nonconserved order parameter, whereas the present problem is actually strictly conserved (mass conservation and immiscibility). To correct this contradiction, a counter term suggested by Folch *et al.* [43] is added on the right-hand side of above equation [12],

$$\partial_t \phi + \boldsymbol{u} \cdot \nabla \phi = M_{\phi} \left(\nabla^2 \phi - \frac{1}{\varepsilon_{\phi}^{2}} \frac{d\psi}{d\phi} - \kappa |\nabla \phi| \right), \tag{7}$$

where the curvature of isocontours can be expressed as $\kappa = \nabla \cdot \boldsymbol{n}$ with $\boldsymbol{n} = \nabla\phi / |\nabla\phi|$. From the asymptotic analysis in Ref. [43], this counter term cancels the curvature dependence of the interfacial equilibrium profile of the interface up to first order. As a result, Eq. (7) relaxes an arbitrary initial phase field to a hyperbolic tangent profile across the interface and then sustains this profile during the interface motion. For the gradient of ϕ at equilibrium state, denoted by θ, one can get the following expressions:

$$\theta = \frac{\partial \phi}{\partial z} = \frac{4(\phi - \phi_h)(\phi - \phi_l)}{W(\phi_l - \phi_h)} \tag{8}$$

and

$$\boldsymbol{n} \cdot \nabla \theta = \frac{\partial^2 \phi}{\partial z^2} = \frac{1}{\varepsilon_\phi^2} \frac{d\psi}{d\phi}. \tag{9}$$

Thus, the last two terms on the right-hand side of Eq. (7) can be rewritten as $-\nabla \cdot (\theta \boldsymbol{n})$. By enforcing the divergence-free condition, the Allen-Cahn equation can be written as [14,30–32]

$$\partial_t \phi + \nabla \cdot (\boldsymbol{u}\phi) = M_\phi \left[\nabla^2 \phi - \nabla \cdot (\theta \boldsymbol{n})\right], \tag{10}$$

which can guarantee the mass conservation exactly with appropriate boundary conditions [14]. The local ACE can also be derived from the interface advection equation or the flux conserving equation, as shown in Refs. [14,31]. The governing equations for the incompressible flows are governed by [28–30]

$$\nabla \cdot \boldsymbol{u} = 0, \tag{11a}$$

$$\rho(\partial_t \boldsymbol{u} + \boldsymbol{u} \cdot \nabla \boldsymbol{u}) = -\nabla p + \nabla \cdot \boldsymbol{\Pi} + \boldsymbol{F}_s + \boldsymbol{F}_b, \tag{11b}$$

where ρ, p, and μ are the density and hydrodynamic pressure and dynamic viscosity, respectively. $\boldsymbol{\Pi} = \mu(\nabla \boldsymbol{u} + \nabla \boldsymbol{u}^T)$ is the viscous stress tensor and $\boldsymbol{F}_b$ is the body force. The surface tension force can be calculated by $\boldsymbol{F}_s = \mu_\phi \nabla \phi$ where the chemical potential μ_ϕ is defined as

$$\mu_\phi = \frac{\delta \mathcal{F}}{\delta \phi} = \frac{d\psi}{d\phi} - \varepsilon_\phi^2 \nabla^2 \phi.$$

B. The MRT-LB model for Allen-Cahn equation

Within the framework of lattice Boltzmann theory, the evolution equation for the order parameter ϕ using multiple-relaxation-time algorithm can be expressed as

$$\begin{aligned} \boldsymbol{h}(\boldsymbol{x} + \boldsymbol{e}\delta_t, t + \delta_t) - \boldsymbol{h}(\boldsymbol{x}, t) = {} & -\mathbf{M}^{-1}\mathbf{S}[\boldsymbol{m}(\boldsymbol{x}, t) - \boldsymbol{m}^{\mathrm{eq}}(\boldsymbol{x}, t)] \\ & + \delta_t \mathbf{M}^{-1}(\mathbf{I} - \mathbf{S}/2)\boldsymbol{q}(\boldsymbol{x}, t). \end{aligned} \tag{12}$$

where $\boldsymbol{m}$, $\boldsymbol{m}^{\mathrm{eq}}$, and $\boldsymbol{q}$ are the moments of distribution function $\boldsymbol{h}$, equilibrium distribution function $\boldsymbol{h}^{\mathrm{eq}}$, and source term $\boldsymbol{q}^\phi$, respectively. $\mathbf{M}$ is the transformation matrix between velocity space and moment space so that we have $\boldsymbol{m} = \mathbf{M}\boldsymbol{h}$, $\boldsymbol{m}^{\mathrm{eq}} = \mathbf{M}\boldsymbol{h}^{\mathrm{eq}}$, and $\boldsymbol{q} = \mathbf{M}\boldsymbol{q}^\phi$. In the following study, the D2Q9 lattice model is adopted and $\mathbf{M}$ can be chosen as [28]

$$\mathbf{M} = \begin{pmatrix} 1 & 1 & 1 & 1 & 1 & 1 & 1 & 1 & 1 \\ -4 & -1 & -1 & -1 & -1 & 2 & 2 & 2 & 2 \\ 4 & -2 & -2 & -2 & -2 & 1 & 1 & 1 & 1 \\ 0 & 1 & 0 & -1 & 0 & 1 & -1 & -1 & 1 \\ 0 & -2 & 0 & 2 & 0 & 1 & -1 & -1 & 1 \\ 0 & 0 & 1 & 0 & -1 & 1 & 1 & -1 & -1 \\ 0 & 0 & -2 & 0 & 2 & 1 & 1 & -1 & -1 \\ 0 & 1 & -1 & 1 & -1 & 0 & 0 & 0 & 0 \\ 0 & 0 & 0 & 0 & 0 & 1 & -1 & 1 & -1 \end{pmatrix}. \tag{13}$$

The weighting coefficients w_i are given by $w_0 = 4/9$, $w_{1\text{–}4} = 1/9$, and $w_{5\text{–}8} = 1/36$ and the lattice vectors e_i are

$$\boldsymbol{e} = \begin{bmatrix} 0 & 1 & 0 & -1 & 0 & 1 & -1 & -1 & 1 \\ 0 & 0 & 1 & 0 & -1 & 1 & 1 & -1 & -1 \end{bmatrix} c, \tag{14}$$

where c is the streaming speed defined as the ratio of lattice length δ_x to time increment δ_t, $c = \delta_x/\delta_t$. The lattice speed of sound is $c_s = c/\sqrt{3}$.

Since only one conserved moment (m_0) exists in the present problem, it is feasible and simple to adopt the linear equilibrium distribution. Besides, without the second-order velocity terms in equilibrium distribution, the deviated term $\frac{M_\phi}{c_s^2} \nabla\nabla : (\phi \boldsymbol{u}\boldsymbol{u})$ can be avoided in the recovered macroscopic equation [32]. Thus, the equilibrium distribution in moment space can be written as

$$\boldsymbol{m}^{eq} = \phi \left[1, \alpha_1, \alpha_2, \frac{\gamma u_x}{c}, -\frac{\gamma u_x}{c}, \frac{\gamma u_y}{c}, -\frac{\gamma u_y}{c}, 0, 0\right]^T, \tag{15}$$

where α_1 and α_2 are free parameters. The moments of source term are given by

$$\boldsymbol{q} = \zeta c \theta [0, 0, 0, n_x, -n_x, n_y, -n_y, 0, 0]^T. \tag{16}$$

The parameters γ and ζ will be determined later through Chapman-Enskog analysis.

To recover the correct macroscopic equation, we introduce an off-diagonal relaxation matrix in the present modified model, which is expressed as

$$\mathbf{S} = \begin{bmatrix} s_0 & s_{01} & s_{02} & 0 & 0 & 0 & 0 & 0 & 0 \\ 0 & s_1 & 0 & 0 & 0 & 0 & 0 & 0 & 0 \\ 0 & 0 & s_2 & 0 & 0 & 0 & 0 & 0 & 0 \\ 0 & 0 & 0 & s_3 & 0 & 0 & 0 & 0 & 0 \\ 0 & 0 & 0 & 0 & s_4 & 0 & 0 & 0 & 0 \\ 0 & 0 & 0 & 0 & 0 & s_5 & 0 & 0 & 0 \\ 0 & 0 & 0 & 0 & 0 & 0 & s_6 & 0 & 0 \\ 0 & 0 & 0 & 0 & 0 & 0 & 0 & s_7 & 0 \\ 0 & 0 & 0 & 0 & 0 & 0 & 0 & 0 & s_8 \end{bmatrix}. \tag{17}$$

Following the parameters choices in Ref. [45], we set $s_3 = s_5 = s_j$, $s_4 = s_6 = s_q$, and $s_7 = s_8 = s_p$. The off-diagonal elements are determined by

$$s_{01} = \frac{\alpha_2}{\alpha_1} \frac{\gamma - 1}{\gamma} s_1 \tag{18}$$

and

$$s_{02} = -\frac{\gamma - 1}{\gamma} s_2. \tag{19}$$

The macroscopic variable ϕ is calculated by

$$\phi = \sum_{i=0}^{8} h_i. \tag{20}$$

Note the basic form of the present MRT-LB model is similar to that of conventional ones, but there is a major difference in the relaxation time matrix. In the conventional MRT-LB models, the diagonal relaxation matrix is adopted instead, which is expressed as $\mathbf{S} = \mathrm{diag}(s_0, s_e, s_\epsilon, s_j, s_q, s_j, s_q, s_p, s_p)$. Table I lists different conventional MRT-LB schemes and their corresponding error term R_ϕ in the recovered macroscopic equation. Among them, MRT-A and MRT-C are the original

TABLE I. The equilibrium distribution function $\boldsymbol{h}^{\mathrm{eq}} = \mathbf{M}^{-1}\boldsymbol{m}^{\mathrm{eq}}$, source term $\boldsymbol{q}^{\phi} = \mathbf{M}^{-1}\boldsymbol{q}$, and the artificial term R_ϕ in different models. In the present model, the weighting coefficients $\bar{w}_i$ are given by $\bar{w}_0 = (1-\alpha_1+\alpha_2)/9$, $\bar{w}_{1-4} = (4-\alpha_1-2\alpha_2)/36$, and $\bar{w}_{5-8} = (4+2\alpha_1+2\alpha_2)/36$.

Model	Equilibrium function h_i^{eq}	Source term q_i^{ϕ}	R_ϕ
MRT-A	$w_i\phi(1+\frac{\boldsymbol{e}_i\cdot\boldsymbol{u}}{c_s^2})$	$w_i\boldsymbol{e}_i\cdot\theta\boldsymbol{n}$	$\frac{M_\phi}{c_s^2}\boldsymbol{\nabla}\cdot\partial_t(\phi\boldsymbol{u})$
MRT-B [32,44]	$w_i\phi(1+\frac{\boldsymbol{e}_i\cdot\boldsymbol{u}}{c_s^2})$	$w_i\frac{\boldsymbol{e}_i\cdot[\partial_t(\phi\boldsymbol{u})+c_s^2\theta\boldsymbol{n}]}{c_s^2}$	0
MRT-C [16,31]	$w_i\phi[1+\frac{\boldsymbol{e}_i\cdot\boldsymbol{u}}{c_s^2}+\frac{(\boldsymbol{e}_i\cdot\boldsymbol{u})^2}{2c_s^4}-\frac{\boldsymbol{u}\cdot\boldsymbol{u}}{2c_s^2}]$	$w_i\boldsymbol{e}_i\cdot\theta\boldsymbol{n}$	$\frac{M_\phi}{c_s^2}\boldsymbol{\nabla}\cdot[\partial_t(\phi\boldsymbol{u})+\boldsymbol{\nabla}\cdot(\phi\boldsymbol{u}\boldsymbol{u})]$
MRT-D	$w_i\phi[1+\frac{\boldsymbol{e}_i\cdot\boldsymbol{u}}{c_s^2}+\frac{(\boldsymbol{e}_i\cdot\boldsymbol{u})^2}{2c_s^4}-\frac{\boldsymbol{u}\cdot\boldsymbol{u}}{2c_s^2}]$	$w_i\frac{\boldsymbol{e}_i\cdot[\partial_t(\phi\boldsymbol{u})+\boldsymbol{\nabla}\cdot(\phi\boldsymbol{u}\boldsymbol{u})+c_s^2\theta\boldsymbol{n}]}{c_s^2}$	0
Present	$\phi(\bar{w}_i+w_i\gamma\frac{\boldsymbol{e}_i\cdot\boldsymbol{u}}{c_s^2})$	$3\zeta w_i\boldsymbol{e}_i\cdot\theta\boldsymbol{n}$	0

forms using linear and nonlinear equilibrium function, respectively. By setting $\alpha_1 = -2$, $\alpha_2 = 1$, $\gamma = 1$, and $\zeta = 1/3$, our model reduces to MRT-A. MRT-B can be considered as the corresponding MRT schemes for Geier's model [31]. The error terms for MRT-A and MRT-C are in the order of $O(\mathrm{Ma}^2)$, which will cause numerical error in the case of large Mach number. To remove the deviated term in MRT-A, a time-dependent source term is added in the modified model [32], denoted as MRT-B here. Using the same strategy, MRT-C with correction term is also presented for comparative studies, labeled by MRT-D. Although both MRT-B and MRT-D satisfy $R_\phi = 0$, the additional source terms introduced need to be computed with nonlocal numerical schemes, which reduces the efficiency of parallel calculation. Our proposed model provides an alternative way to recover the correct macroscopic equation. The off-diagonal relaxation matrix $\mathbf{S}$ produces diffusion effects to eliminate artificial term without sacrificing locality of the model. From the computational point of view, the existence of off-diagonal elements has little effect on the implementation of MRT-LB model. The slight difference lies in the collision step of m_0, i.e.,

$$\begin{aligned} m_0^* = s_0\big(m_0 - \bar{m}_0^{\mathrm{eq}}\big) + s_{01}\big(m_1 - \bar{m}_1^{\mathrm{eq}}\big) \\ + s_{02}\big(m_2 - \bar{m}_2^{\mathrm{eq}}\big) + \delta_t q_0, \end{aligned} \tag{21}$$

where $\bar{\boldsymbol{m}}^{\mathrm{eq}} = \boldsymbol{m}^{\mathrm{eq}} - \delta_t\boldsymbol{q}/2$ and the additional terms related to s_{01} and s_{02} will make the present model a little more expensive.

C. Chapman-Enskog analysis

Next, the Chapman-Enskog analysis will be conducted to recover Eq. (10) by the present modified model. The second-order Taylor series expansion of the evolution equation Eq. (12) yields

$$\boldsymbol{D}\boldsymbol{m} + \frac{\delta_t}{2}\boldsymbol{D}^2\boldsymbol{m} + O\big(\delta_t^2\big) = -\frac{\mathbf{S}}{\delta_t}(\boldsymbol{m} - \boldsymbol{m}^{\mathrm{eq}}) + \left(\mathbf{I} - \frac{\mathbf{S}}{2}\right)\boldsymbol{q}, \tag{22}$$

where $\boldsymbol{D} = \mathbf{I}\partial_{t1} + \boldsymbol{E}\cdot\boldsymbol{\nabla}$ and $\boldsymbol{E} = (\boldsymbol{E}_x, \boldsymbol{E}_y)$ can be expressed as

$$\begin{aligned} \boldsymbol{E}_x &= \mathbf{M}[\mathrm{diag}\,(e_{0x}, e_{1x}, \ldots, e_{8x})]\mathbf{M}^{-1}, \\ \boldsymbol{E}_y &= \mathbf{M}[\mathrm{diag}\,(e_{0y}, e_{1y}, \ldots, e_{8y})]\mathbf{M}^{-1}. \end{aligned} \tag{23}$$

The following multiscale expansions are applied,

$$\begin{aligned} &\partial_t = \varepsilon\partial_{t1} + \varepsilon^2\partial_{t2}, \qquad \nabla = \varepsilon\nabla_1, \\ &\boldsymbol{m} = \boldsymbol{m}^{(0)} + \varepsilon\boldsymbol{m}^{(1)} + \varepsilon^2\boldsymbol{m}^{(2)} + \ldots, \qquad \boldsymbol{q} = \varepsilon\boldsymbol{q}^{(1)}. \end{aligned} \tag{24}$$

Substituting these expansions into Eq. (22), the evolution equation can be reorganized in the consecutive orders of ε as

$$\varepsilon^0 : \boldsymbol{m}^{(0)} = \boldsymbol{m}^{\mathrm{eq}}, \tag{25a}$$

$$\varepsilon^1 : \boldsymbol{D}_1\boldsymbol{m}^{(0)} - \boldsymbol{q}^{(1)} = -\frac{\mathbf{S}}{\delta_t}\left[\boldsymbol{m}^{(1)} + \frac{\delta_t}{2}\boldsymbol{q}^{(1)}\right], \tag{25b}$$

$$\varepsilon^2 : \partial_{t2}\boldsymbol{m}^{(0)} + \boldsymbol{D}_1\left(\mathbf{I} - \frac{1}{2}\mathbf{S}\right)\left[\boldsymbol{m}^{(1)} + \frac{\delta_t}{2}\boldsymbol{q}^{(1)}\right] = -\frac{\mathbf{S}}{\delta_t}\boldsymbol{m}^{(2)}, \tag{25c}$$

where $\boldsymbol{D}_1 = \mathbf{I}\partial_{t1} + \boldsymbol{E}\cdot\boldsymbol{\nabla}_1$. Equation (25a) indicates that

$$m_0^{(i)} = 0, \quad i \geqslant 1. \tag{26}$$

The explicit expression of Eq. (25b) can be written as

$$\begin{bmatrix} \partial_{t1}\phi + \gamma\boldsymbol{\nabla}_1\cdot(\phi\boldsymbol{u}) \\ \alpha_1\partial_{t1}\phi \\ \alpha_2\partial_{t1}\phi - \gamma\boldsymbol{\nabla}_1\cdot(\phi\boldsymbol{u}) \\ \frac{\gamma}{c}\partial_{t1}\phi u_x + \frac{4+\alpha_1}{6}c\partial_{x1}\phi - q_3 \\ -\frac{\gamma}{c}\partial_{t1}\phi u_x + \frac{\alpha_1+\alpha_2}{3}c\partial_{x1}\phi - q_4 \\ \frac{\gamma}{c}\partial_{t1}\phi u_y + \frac{4+\alpha_1}{6}c\partial_{y1}\phi - q_5 \\ -\frac{\gamma}{c}\partial_{t1}\phi u_y + \frac{\alpha_1+\alpha_2}{3}c\partial_{y1}\phi - q_6 \\ \frac{2\gamma}{3}\partial_{x1}\phi u_x - \frac{2\gamma}{3}\partial_{y1}\phi u_y \\ \frac{\gamma}{3}\partial_{x1}\phi u_y + \frac{\gamma}{3}\partial_{y1}\phi u_x \end{bmatrix} = -\frac{\mathbf{S}}{\delta_t}\begin{bmatrix} 0 \\ m_1^{(1)} \\ m_2^{(1)} \\ m_3^{(1)} + \frac{\delta_t}{2}q_3 \\ m_4^{(1)} + \frac{\delta_t}{2}q_4 \\ m_5^{(1)} + \frac{\delta_t}{2}q_5 \\ m_6^{(1)} + \frac{\delta_t}{2}q_6 \\ m_7^{(1)} \\ m_8^{(1)} \end{bmatrix}. \tag{27}$$

To simplify analysis, the left-hand side of Eq. (27) can be considered as a vector, $\boldsymbol{L} = \boldsymbol{D}_1\boldsymbol{m}^{(0)} - \boldsymbol{q}^{(1)}$, with nine elements. The ith element within the vector is expressed as $L_i = [\boldsymbol{L}]|_{l_i}$, for instance, $[\boldsymbol{L}]|_{l_1} = \partial_{t1}\phi + \gamma\boldsymbol{\nabla}_1\cdot(\phi\boldsymbol{u})$. Here we define a linear operation Ψ among the vector elements as $[\boldsymbol{L}]|_{\Psi(l_i)} = \Psi(L_i)$. Due to the off-diagonal relaxation matrix $\mathbf{S}$, the first equation in Eq. (27) is related to $m_1^{(1)}$ and $m_2^{(1)}$. Using the linear operation, $\Psi(l_i) = l_0 - \frac{s_{01}}{s_1}l_1 - \frac{s_{02}}{s_2}l_2$, then the first equation can be expressed as

$$[\boldsymbol{L}]|_{\Psi(l_i)} = L_0 - \frac{s_{01}}{s_1}L_1 - \frac{s_{02}}{s_2}L_2 = 0, \tag{28}$$

which can be organized as

$$\left(1 - \frac{\alpha_1 s_{01}}{s_1} - \frac{\alpha_2 s_{02}}{s_2}\right)\partial_{t1}\phi + \left(\gamma + \frac{\gamma s_{02}}{s_2}\right)\boldsymbol{\nabla}_1\cdot(\phi\boldsymbol{u}) = 0. \tag{29}$$

According to Eqs. (18) and (19), one can obtain the first-order equation as

$$\partial_{t1}\phi + \nabla_1 \cdot (\phi \boldsymbol{u}) = 0. \tag{30}$$

Similarly, by enforcing the same linear operation Ψ at the ε^2 scale, the first equation in Eq. (25c) is written as

$$[\partial_{t2}\boldsymbol{m}^{(0)} + (\mathbf{I}\partial_{t1} + \boldsymbol{E} \cdot \nabla_1)\boldsymbol{L}^{(1)}]|_{\Psi} = 0, \tag{31}$$

where the vector $\boldsymbol{L}^{(1)} = (\mathbf{I} - \mathbf{S}/2)[\boldsymbol{m}^{(1)} + \delta_t \boldsymbol{q}^{(1)}/2]$. Using Eqs. (25b) and (28) gives

$$L_i^{(1)} = \begin{cases} \delta_t L_0/2, & i = 0, \\ \delta_t L_i(1/2 - 1/s_i), & i \neq 0. \end{cases} \tag{32}$$

Utilizing the relation, $\alpha_1 s_{01} + \alpha_2 s_{02} = 0$, the first term in Eq. (31) yields

$$[\partial_{t2}\boldsymbol{m}^{(0)}]|_{\Psi} = \partial_{t2}\phi. \tag{33}$$

Substituting Eq. (32) into Eq. (31), the next two terms can be expressed as

$$[\partial_{t1}\boldsymbol{L}^{(1)}]|_{\Psi} = \eta_1 \partial_{t1} \nabla_1 \cdot (\phi \boldsymbol{u}) \tag{34}$$

and

$$\begin{aligned}[\boldsymbol{E} \cdot \nabla_1 \boldsymbol{L}^{(1)}]|_{\Psi} = &-M_\phi \nabla_1^2 \phi \\ &+ \eta_2 \nabla_1 \cdot [\partial_{t1}(\phi \boldsymbol{u}) - c^2 \zeta \theta \boldsymbol{n}/\gamma],\end{aligned} \tag{35}$$

where η_1 is determined by

$$\eta_1 = \delta_t \left(\frac{\alpha_2 + \gamma}{s_2} - \frac{\alpha_2}{s_1}\right)\frac{\gamma - 1}{\gamma} \tag{36}$$

and M_ϕ and η_2 are related to relaxation times s_j and s_q by

$$\eta_2 = -\delta_t \left[\left(s_j^{-1} - 0.5\right) + \frac{\alpha_2 - \alpha_1}{\alpha_1}\left(s_q^{-1} - s_j^{-1}\right)(\gamma - 1)\right] \tag{37}$$

and

$$\begin{aligned} M_\phi = c^2 \delta_t \Bigg[&\left(s_j^{-1} - 0.5\right)\left(1 - \frac{s_{01}}{s_1}\right)\frac{4 + \alpha_1}{6} \\ &-\left(s_q^{-1} - 0.5\right)\left(\frac{s_{01}}{s_1} + \frac{s_{02}}{s_2}\right)\frac{\alpha_1 + \alpha_2}{3}\Bigg]. \end{aligned} \tag{38}$$

In order to obtain the second-order equation as

$$\partial_{t2}\phi = M_\phi \nabla_1 \cdot [\nabla_1 \phi - \theta \boldsymbol{n}], \tag{39}$$

the following constraints need to be satisfied:

$$\zeta c^2 \eta_2/\gamma = -M_\phi \tag{40}$$

and

$$\eta_1 + \eta_2 = 0. \tag{41}$$

Combined equations Eqs. (30) and (39), the macroscopic equation can be exactly recovered as Eq. (10).

Following the similar procedure, the macroscopic equations with or without error terms can also be recovered for different MRT-LB models in Table I. For these conventional MRT-LB schemes, the moment vectors are decoupled and the linear operation is simplified as $\Psi(l_i) = l_0$. Then the term in Eq. (34) equals zero and the deviation terms emerged from Eq. (35) will be retained in MRT-A and MRT-C but will be removed in MRT-B and MRT-D by introducing additional source terms. The off-diagonal relaxation matrix for present MRT-LB model provides an alternative way to cancel out such deviation term by producing the term of $\eta_1 \partial_{t1} \nabla_1 \cdot (\phi \boldsymbol{u})$. It should be noted that this strategy is not suitable for the case with nonlinear equilibrium function. In that case, the unwanted terms of $\partial_k \partial_l (\phi u_k u_l)$ will emerge in Eq. (35), which cannot be removed thoroughly by the present modified model. The parameters $s_1, s_2, s_j, s_q, \gamma, \alpha_1$, and α_2 could have different choices as long as they are satisfied the relations in Eqs. (38) and (41). One simple choice is to set $s_1 = s_2 = s_e$, $s_q = s_j$, $\alpha_1 = -4 + 2\Gamma$, and $\alpha_2 = 4 - 3\Gamma$, where Γ is freely adjusted to improve the stability and accuracy. Based on Eqs. (38), (40), and (41), we have

$$M_\phi = \frac{\Gamma}{3\gamma} c^2 (1/s_j - 0.5)\delta_t, \tag{42}$$

$$\zeta = \Gamma/3, \tag{43}$$

and

$$\gamma = 1 + s_\epsilon (1/s_j - 0.5). \tag{44}$$

According to Eq. (42), s_j in the present model is determined by the mobility M_ϕ, the relaxation factor s_e, and parameter Γ, which allows more flexibility in the design of relaxation matrix.

D. The MRT-LB model for hydrodynamic equations

The discrete Boltzmann equation for the pressure distribution function f_i with a general forcing term F_i is written as [28,46]

$$\partial_t f_i + \boldsymbol{e}_i \cdot \nabla f_i = \Omega_f + F_i, \tag{45}$$

where the collision term is $\Omega_f = -\Lambda_{ij}(f_j - f_j^{\text{eq}})$. The equilibrium distribution function f_i^{eq} is given by

$$f_i^{\text{eq}} = \begin{cases} (w_0 - 1)p + \rho c_s^2 s_0(\boldsymbol{u}), & i = 0, \\ w_i p + \rho c_s^2 s_i(\boldsymbol{u}), & i \neq 0, \end{cases} \tag{46}$$

where

$$s_i(\boldsymbol{u}) = w_i \left[\frac{\boldsymbol{e}_i \cdot \boldsymbol{u}}{c_s^2} + \frac{(\boldsymbol{e}_i \cdot \boldsymbol{u})^2}{2c_s^4} - \frac{\boldsymbol{u}^2}{2c_s^2}\right].$$

The density of the fluid is obtained from the phase field

$$\rho = \rho_l + \frac{\phi - \phi_l}{\phi_h - \phi_l}(\rho_h - \rho_l), \tag{47}$$

where ρ_h and ρ_l are the densities of the heavy and light fluids, respectively. The discrete forcing term is [28]

$$F_i = (\boldsymbol{e}_i - \boldsymbol{u}) \cdot \left\{ s_i(\boldsymbol{u}) c_s^2 \nabla \rho + [s_i(\boldsymbol{u}) + w_i](\boldsymbol{F}_s + \boldsymbol{F}_b + \boldsymbol{F}_a) \right\}. \tag{48}$$

where $\boldsymbol{F}_a = q\boldsymbol{u} = \frac{\rho_h - \rho_l}{\phi_h - \phi_l} M_\phi \nabla \cdot (\nabla \phi - \theta \boldsymbol{n})\boldsymbol{u}$ is the interfacial force. To get an explicit discretized version of Eq. (45), the following modified distribution function is used:

$$\bar{f}_i = f_i - \frac{\delta_t}{2}(\Omega_f + F_i). \tag{49}$$

Then the modified equilibrium distribution function becomes

$$\bar{f}_i^{\text{eq}} = f_i^{\text{eq}} - \frac{\delta_t}{2} F_i. \tag{50}$$

From Eqs. (49) and (50), we obtain

$$\bar{f}_i - \bar{f}_i^{\rm eq} = [\mathbf{I} + \delta_t \Lambda/2]_{ij}\big(f_j - f_j^{\rm eq}\big). \tag{51}$$

The final form of evolution function reads as

$$\bar{f}_i(\boldsymbol{x} + \boldsymbol{e}_i\delta_t, t + \delta_t) - \bar{f}_i(\boldsymbol{x}, t) = -\bar{\Lambda}_{ij}\big(\bar{f}_j - \bar{f}_j^{\rm eq}\big) + \delta_t F_i, \tag{52}$$

where $\bar{\Lambda}_{ij}$ satisfies $\bar{\Lambda} = \delta_t \Lambda[\mathbf{I} + \delta_t\Lambda/2]^{-1}$. Within the MRT framework, $\bar{\Lambda}$ is replaced by $\mathbf{M}^{-1}\mathbf{S}^f\mathbf{M}$, where $\mathbf{S}^f$ is a diagonal matrix and expressed as $\mathbf{S}^f = \mathrm{diag}(s_0^f, s_1^f, s_2^f, \ldots, s_8^f)$. The parameters s_7^f and s_8^f are defined as $s_7^f = s_8^f = 1/\tau_f$, where τ_f is related to the dynamic viscosity by

$$\tau_f = \frac{\mu}{\rho c_s^2 \delta_t} + 0.5. \tag{53}$$

Using a linear interpolation, one can obtain the dynamic viscosity μ as [47]

$$\mu = \mu_l + \frac{\phi - \phi_l}{\phi_h - \phi_l}(\mu_h - \mu_l), \tag{54}$$

where μ_h and μ_l are the viscosity of the heavy and light phases, respectively. The macroscopic variables are calculated by

$$\boldsymbol{u} = \left[\frac{\sum \boldsymbol{e}_i \bar{f}_i}{c_s^2} + 0.5\delta_t(\boldsymbol{F}_s + \boldsymbol{F}_b)\right]\Big/(\rho - 0.5\delta_t q), \tag{55a}$$

$$p = \frac{1}{1 - w_0}\left[\sum_{i\neq 0} \bar{f}_i + \frac{c_s^2}{2}\delta_t \mathbf{u}\cdot\nabla\rho + \rho c_s^2 s_0(\boldsymbol{u})\right]. \tag{55b}$$

We note the gradient and Laplacian operators exist in the present model, which increases the complexity to implement. Based on the relation in Eq. (47), the gradient of density can be reduced to compute $\nabla\phi$. Using the isotropic central schemes, the gradient and Laplacian of ϕ are calculated by

$$\nabla\phi = \frac{1}{c_s^2\delta_t}\sum_i \boldsymbol{e}_i w_i \phi(x + \boldsymbol{e}_i\delta_t, t) \tag{56}$$

and

$$\nabla^2\phi = \frac{2}{c_s^2\delta_t^2}\sum_i w_i[\phi(x + \boldsymbol{e}_i\delta_t, t) - \phi(x, t)]. \tag{57}$$

The directional derivatives $\boldsymbol{e}_i\cdot\nabla\phi$ that appear in the calculation of F_i in Eq. (50) and (52) are calculated by central and mixed finite differences of ϕ, noted by superscripts c and m on the gradient operators, respectively. Their expressions are given by [38]

$$\delta_t\boldsymbol{e}_i\cdot\nabla^c\phi|_{(\boldsymbol{x},t)} = \frac{\phi(\boldsymbol{x} + \mathbf{e}_i\delta_t, t) - \phi(\boldsymbol{x} - \mathbf{e}_i\delta_t, t)}{2} \tag{58}$$

and

$$\begin{aligned}\delta_t\boldsymbol{e}_i\cdot\nabla^m\phi|_{(\boldsymbol{x},t)} = &-\frac{1}{4}[\phi(\boldsymbol{x} - \mathbf{e}_i\delta_t, t) + 3\phi(\boldsymbol{x}, t)\\ &-5\phi(\boldsymbol{x} + \mathbf{e}_i\delta_t, t) + \phi(\boldsymbol{x} + 2\mathbf{e}_i\delta_t, t)].\end{aligned} \tag{59}$$

Previous studies have analyzed the effects of force discretization using isotropic central scheme (ICS) and mixed scheme (MS). The mixed scheme is shown to violate the exact mass and momentum conservation [48–50]. However, as reported in Ref. [51], the nonconservative forcing terms seem to have negligible effects for the actual dynamics. Here we checked the mass conservation in the case of static drop system. Different from the findings in Ref. [49], both central and mixed schemes in the present phase-field-based LB model are able to guarantee the mass conservation very well.

III. NUMERICAL TESTS FOR INTERFACE CAPTURING

In this section, we will check the performance of the proposed MRT-LB model for the interface capturing. In the following tests, velocity fields have been prespecified and only the Allen-Cahn equation is solved. The conventional MRT-LB schemes presented in Table I are also adopted for comparative studies. Through the Chapman-Enskog analysis at ε^3 scale, the leading error term for the conventional MRT-LB models can be written as

$$R_{\phi 3} = -\left(s_j^{-1} - \frac{1}{2}\right)\big(s_e^{-1} + s_p^{-1} - 1\big)c_s^2\delta_t^2\nabla^2\nabla\cdot\phi\boldsymbol{u}. \tag{60}$$

To make the comparative analysis simple and convincing, we fix $s_p = 1$ and take different choices of s_e to consider the effect of high-order error terms. Other relaxation parameters can be chosen freely within an appropriate range. Here we set $s_0 = 1$, $s_2 = s_1 = s_e$, and $s_q = s_j$. In conventional MRT-LB models, s_j is chosen as $s_j = 1/\tau_h$, where τ_h is uniquely determined by the mobility based on $M_\phi = (\tau_h - 0.5)c_s^2\delta_t$. For the present MRT model, two free parameters, i.e., s_e and Γ (or s_j), exist to tune the stability and accuracy according to Eq. (42). Once s_e and s_j are given, the off-diagonal elements can be obtained. The phase field is initialized by its equilibrium state. Ideally, the order parameter should be bounded between ϕ_l and ϕ_h during the simulation. However, strict boundedness of ϕ is hard to achieve due to numerical dispersion. To quantitatively evaluate the numerical dispersion, the relative maximum and minimum values of order parameter are introduced and defined as [32]

$$\bar{\phi}_{\max} = \frac{\phi_{\max} - \phi_h}{\phi_h - \phi_l}, \quad \bar{\phi}_{\min} = \frac{\phi_{\min} - \phi_l}{\phi_h - \phi_l}. \tag{61}$$

The numerical accuracy is described by the relative error of ϕ, i.e.,

$$\mathrm{Er} = \frac{\sum_{\boldsymbol{x}} |\phi(\boldsymbol{x}, T) - \phi(\boldsymbol{x}, 0)|}{\sum_{\boldsymbol{x}} |\phi(\boldsymbol{x}, 0)|}. \tag{62}$$

A. Zalesak's rotation

The Zalesak's rotation is widely used to measure the numerical accuracy of interface-capturing techniques in maintaining sharp corners. A notched disk of radius 80 and notch width 16 is initially placed in the center of a $L_0 \times L_0$ box. The imposed velocity field is given by [31]

$$u = -U_0\pi\left(\frac{y}{L_0} - 0.5\right), \quad v = U_0\pi\left(\frac{x}{L_0} - 0.5\right), \tag{63}$$

where $L_0 = 200$. Different from the periodic boundary adopted in Refs. [26,28,31] the nonequilibrium extrapolation boundary condition is employed here to avoid the singularity emerged at the corner. Theoretically, the disk will maintain its shape during the rotation and return to the initial condition

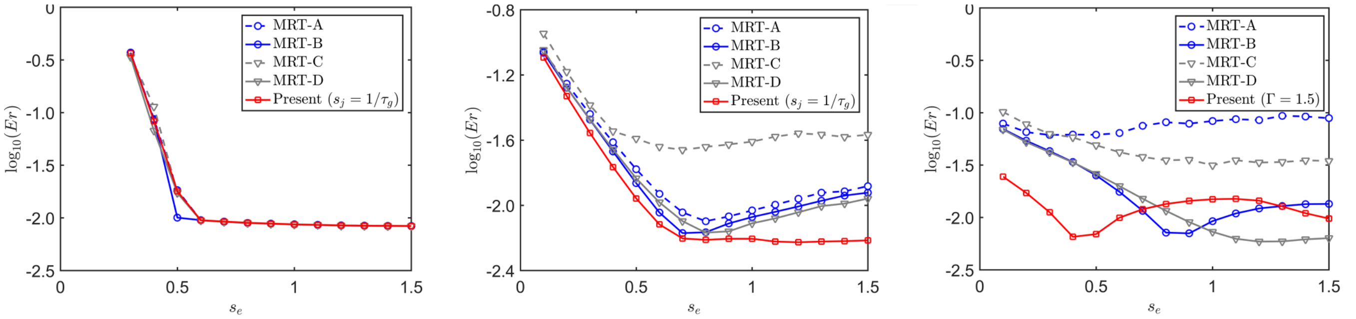

(a) (b) (c)

FIG. 1. Comparisons of the relative errors of different MRT-LB models for the cases at (a) $U = 0.025$, $M_\phi = 0.001$; (b) $U = 0.1$, $M_\phi = 0.1$; and (c) $U = 0.25$, $M_\phi = 0.1$.

at $T = 2L_0/U_0$. In this test, phase interface width and surface tension are fixed at $W = 2$ and $\sigma = 0.04$, respectively. The phase indicators are $\phi_h = 1$ and $\phi_l = -1$. A comparative study on different LB models will be presented below.

First, we conduct the simulation at $U_0 = 0.025$ and $M_\phi = 0.001$. In this case, all these above mentioned models are able to capture a stable and accurate interface after one period. Relative errors for the MRT models at various s_e are plotted in Fig. 1(a). Compared with their corresponding SRT schemes, these MRT models have very limited improvement on the numerical accuracy. On the contrary, as $s_e \leqslant 0.5$, artificial diffusion occurs and the interfaces become instability. Note that the curves of $\log_{10}(\mathrm{Er})$ versus s_e for different MRT models are coincided with each other, which implies the additional artificial terms can be ignored in such condition.

Since the deviation terms in MRT-A and MRT-C are in the order of $O(\mathrm{Ma}^2)$, to show the effect of this term clearly, two cases with larger velocity are studied. The mobility is fixed at $M_\phi = 0.1$ and the velocity is set as $U = 0.1$ and $U = 0.25$, respectively. The relative errors for different MRT-LB models at varied relaxation parameter s_e are presented in Figs. 1(b) and 1(c). It can be seen that the accuracy of these MRT-LB models are affected greatly by the relaxation factor s_e. Both the present model and the MRT-LB schemes with correction (i.e., MRT-B and MRT-D) have smaller relative errors than the conventional ones without correction (i.e., MRT-A and MRT-C). For the case of $U = 0.1$, MRT-C produces the largest numerical errors, which seems counterintuitive that the nonlinear equilibrium function performs worse than the linear one. This can be explained by the additional error term in MRT-C. Once the correction terms added, such counterintuitive phenomenon is disappeared between MRT-B and MRT-D. Among these modified MRT-LB schemes, our present model has better performance than MRT-B and MRT-D, especially when s_e is in the range of 1.0 to 1.5. As the velocity increases to $U = 0.25$, MRT-A and MRT-C fail to obtain the phase field within an acceptable error range. On the contrary, by carefully setting the value of s_e, we could reduce the relative errors to 7.05×10^{-3} for MRT-B, 5.89×10^{-3} for MRT-D and 6.53×10^{-3} for our proposed model, respectively, which shows the necessity to remove those deviation terms. Figure 2 shows the phase interfaces after one period obtained by different MRT-LB schemes for the case of $U = 0.25$. The relaxation parameter s_e is set as 0.8 in MRT-A and MRT-B, 1.2 in MRT-C and MRT-D, and 0.4 in the present model so that all these models presents their best performances. To show the artificial diffusion better, the contours are displayed within a range of $-0.9 \leqslant \phi \leqslant 0.9$. For the interface obtained by MRT-A, we observe the slot is obviously slanted and the circular interface is serrated at small s_e. As s_e increases, the serrated interface will spread to the whole circle interface, as shown in Fig. 2(a). The jagged interface can be avoided in MRT-C by using nonlinear equilibrium function, but unphysical diffusion will emerge due to the additional error term $\frac{M_\phi}{c_s^2}\nabla\nabla : (\phi \boldsymbol{uu})$. After introducing the correction source terms, stable phase interfaces can be obtained by MRT-B and the artificial diffusion can be avoided in MRT-D. Using our newly proposed model, a stable and accurate interface can also be obtained, as shown in Fig. 2(e). Relative minimum and maximum values of ϕ at time T for the case of $U = 0.25$ are listed in Table II. It is shown that both $\bar{\phi}_{\max}$ and $|\bar{\phi}_{\min}|$ in the present model are smaller than the conventional MRT-LB models. These tests demonstrate that without the deviation terms, the present modified MRT model shows superiority in reducing relative error and dispersion error under the condition of relatively large velocity.

B. Drop in shear flow

To check the performance in capturing the complex deformation of phase boundaries, a two-dimensional (2D) circular interface with radius $R = L_0/5$ is placed in the center of a $L_0 \times L_0$ box with an imposed velocity field [32],

$$u = -U_0 \sin\left(\frac{4\pi x}{L_0}\right) \times \sin\left(\frac{4\pi y}{L_0}\right) \cos\frac{\pi t}{T},$$
$$v = -U_0 \cos\left(\frac{4\pi x}{L_0}\right) \times \cos\left(\frac{4\pi y}{L_0}\right) \cos\frac{\pi t}{T}, \tag{64}$$

where L_0 is fixed at 500. The period time is defined as $T = 1.25L_0/U_0$. The parameters ϕ_h, ϕ_l, W and σ are set the same as those in Zalesak's disk test.

We compared the present MRT model with other conventional MRT-LB schemes by enforcing $U = 0.25$ and $M_\phi = 0.1$. By using the present MRT model, interface evolutions in one period are depicted in Fig. 3 with an interval of $T/8$. The circle is continuously stretched by the vortices during the first half period and formed a thin filament at time $T/2$. Then the vortices rotate in opposite direction and the thin filament moves back to the initial configuration at time T due to the periodic nature of the flow field. From Fig. 3(h), we

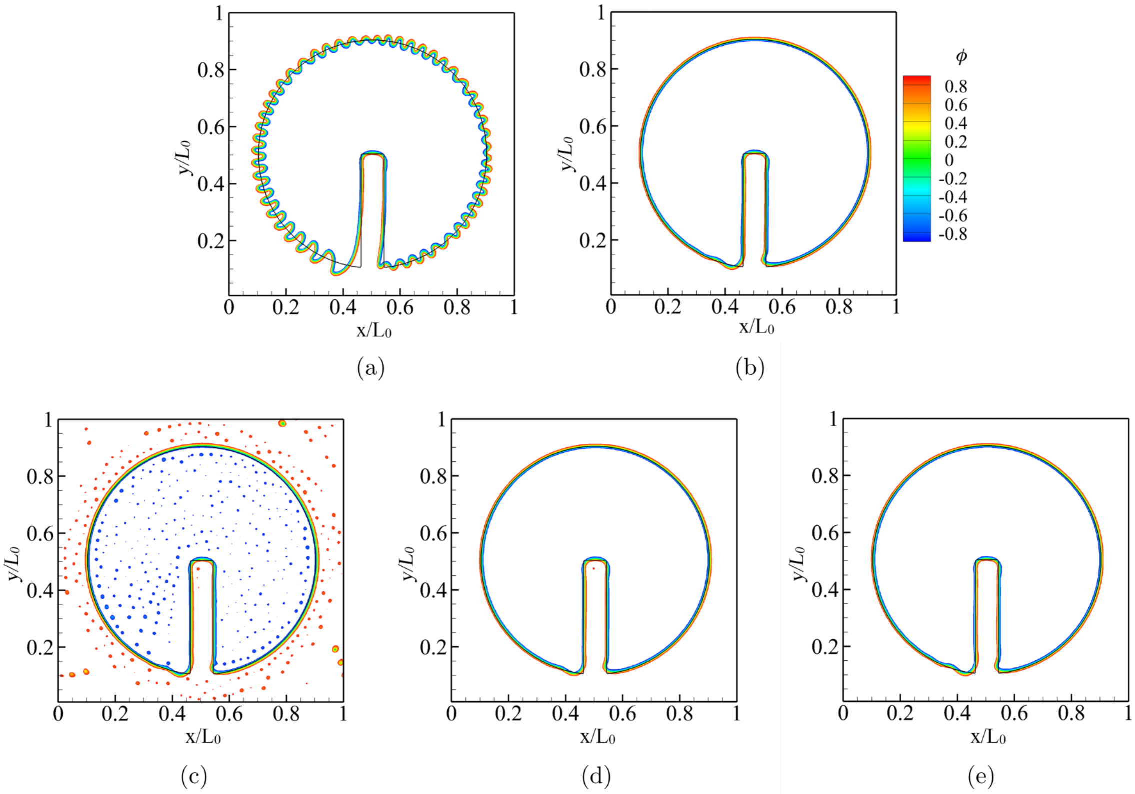

(a) (b)

(c) (d) (e)

FIG. 2. Comparisons of the interface shapes after one period at $U = 0.25$ obtained by (a) MRT-A, (b) MRT-B, (c) MRT-C, (d) MRT-D, and (e) the present model. The contours for phase field are displayed within a range of -0.9 to 0.9.

find that the final profile after one period agrees well with the initial state. Figure 4 plots the effects of adjustable relaxation parameter s_e for different models at time $t = 2T$. Once again, MRT-C presents the largest numerical errors and the counterintuitive phenomenon between MRT-A and MRT-C happens. By adding the correction terms, both MRT-B and MRT-D are able to reduce the numerical errors effectively. For MRT-B, the relative error has a minimum value of 1.03×10^{-3} at $s_e = 0.8$, while the minimum value for MRT-D is 1.02×10^{-3} at $s_e = 0.9$. Our present model maintains relatively low numerical errors within a wide range of s_e from 0.6 to 1.5. Phase interfaces obtained by different MRT-LB schemes at $s_e = 0.6$ are plotted in Fig. 5. We note the phase interface is slightly distorted in MRT-A and obvious artificial diffusion occurs in MRT-C. It should be pointed out that the error terms in MRT-C will have more obvious effects on the phase interface evolution in the case of $\phi_h + \phi_l \neq 0$. For instance, if we set $\phi_h = 1$ and $\phi_l = 0$ instead, then the interface shape obtained by MRT-C after one period will become much more distorted, as shown in Fig. 6. For this case, the artificial diffusion is disappeared inside the circle due to $\phi \approx 0$ in that region. All these modified models can capture a stable and accurate interface, whether $\phi_h + \phi_l$ equals zero or not. The effects of numerical dispersion on $\bar{\phi}_{\min}$ and $\bar{\phi}_{\max}$ are listed in Table III. Again, our present modified MRT-LB model is able to reduce the numerical dispersion to some extent.

IV. NUMERICAL TESTS FOR MULTIPHASE FLOWS

As the interface capturing coupled to the Navier-Stokes equations, four dimensionless parameters are introduced to describe physical multiphase fluid, i.e., the density ratio $\lambda_\rho = \rho_h/\rho_l$, the viscosity ratio $\lambda_\mu = \mu_h/\mu_l$, the Reynolds number $\mathrm{Re} = \rho_h U_0 L_0/\mu_h$, and the Eötvös number $\mathrm{Eo} = \rho_h U_0^2 L_0/\sigma$, where U_0 and L_0 are the velocity and length scales, respectively. For a better comparison with available data reported in literature, the Péclet number $\mathrm{Pe} = U_0 L_0/M_\phi$, and the Cahn number $\mathrm{Cn} = W/L_0$ for the phase-field equation will be used.

A. Static drop test

The static drop is a fundamental test to validate the numerical model for the multiphase flows. Here we simulate a 2D

TABLE II. Relative minimum and maximum values of ϕ, $[\bar{\phi}_{\min}, \bar{\phi}_{\max}]$, for Zalesak's disk tests at $U = 0.25$.

s_e	MRT-A	MRT-B	MRT-C	MRT-D	Present
0.4	[−0.096, 0.077]	[−0.058, 0.048]	[−0.056, 0.053]	[−0.053, 0.046]	[−0.039, 0.032]
0.8	[−0.085, 0.101]	[−0.043, 0.037]	[−0.042, 0.037]	[−0.037, 0.032]	[−0.030, 0.019]
1.2	[−0.084, 0.097]	[−0.031, 0.024]	[−0.032, 0.030]	[−0.026, 0.021]	[−0.015, 0.017]

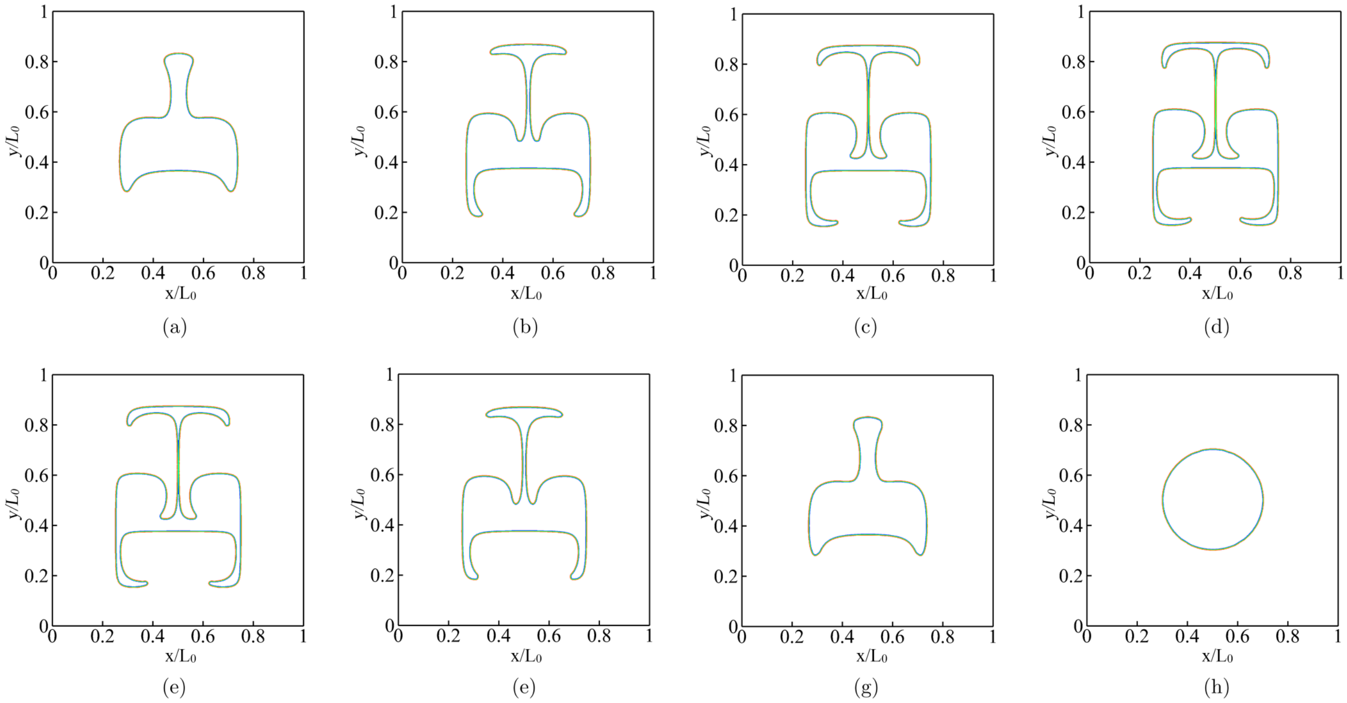

(a) (b) (c) (d)

(e) (e) (g) (h)

FIG. 3. Interface evolution in one period for the present MRT model at $s_e = 0.4$.

drop centered at a square box. The width of the computational domain is $L_0 = 256$ and the radius of drop is $R = 64$. The coordinates of the drop center is $(0, 0)$. All the boundaries are set to be periodic. The phase field is initialized by its equilibrium state and correspondingly the initial density field is given by

$$\rho(x, y) = \frac{\rho_h + \rho_l}{2} + \frac{\rho_h - \rho_l}{2} \tanh\left(2\frac{R - \sqrt{x^2 + y^2}}{W}\right). \tag{65}$$

For the present modified MRT-LB model, we fixed $M_\phi = 0.01$, $s_e = 0.3$, and $\Gamma = 1$. Other computational parameters are set the same as those in Ref. [49], i.e., the drop density $\rho_h = 1$, the vapor density $\rho_l = 0.2$, the Cahn number Cn $= 0.04$, kinematic viscosity $\nu = (\tau_f - 0.5)c_s^2\delta_t = 0.2$, and the coefficient $\beta = 0.01$. To check the effects of force discretization, we will test four different schemes, i.e., MRT-B with the isotropic central scheme (MRT-B-ICS), MRT-B with the mixed scheme (MRT-B-MS), the present model with the isotropic central scheme (present-ICS) and the present model with the mixed scheme (present-MS). Figure 7 presents the spurious currents at $t = 1 \times 10^6\delta_t$, when the equilibrium state has been reached. The magnitude of spurious currents are of $O(10^{-7})$ for all four schemes. As the same force discretization adopted, no obvious differences for the spurious currents are observed between MRT-B and the present model. Different from the results obtained by mixed schemes, the spurious current using isotropic central schemes are only confined to the interface vicinity and have little effect on the bulk phases. The density profiles from the drop center to the

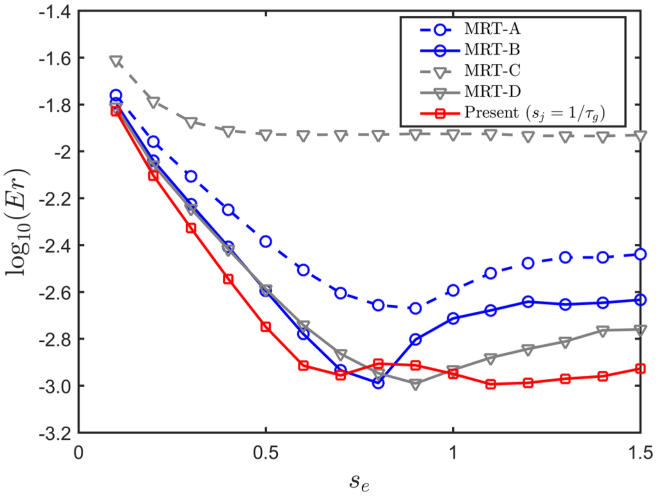

FIG. 4. Comparisons of the relative errors of different MRT-LB models at $U = 0.25$.

TABLE III. Relative maximum and minimum values of ϕ, $[\bar{\phi}_{\min}, \bar{\phi}_{\max}]$, for a drop in shear flow ($U = 0.25$).

s_e	MRT-A	MRT-B	MRT-C	MRT-D	Present
0.4	[−0.062, 0.067]	[−0.047, 0.050]	[−0.048, 0.049]	[−0.045, 0.048]	[−0.036, 0.037]
0.8	[−0.042, 0.080]	[−0.025, 0.024]	[−0.029, 0.029]	[−0.023, 0.025]	[−0.013, 0.015]
1.2	[−0.029, 0.031]	[−0.015, 0.017]	[−0.020, 0.020]	[−0.014, 0.014]	[−0.005, 0.006]

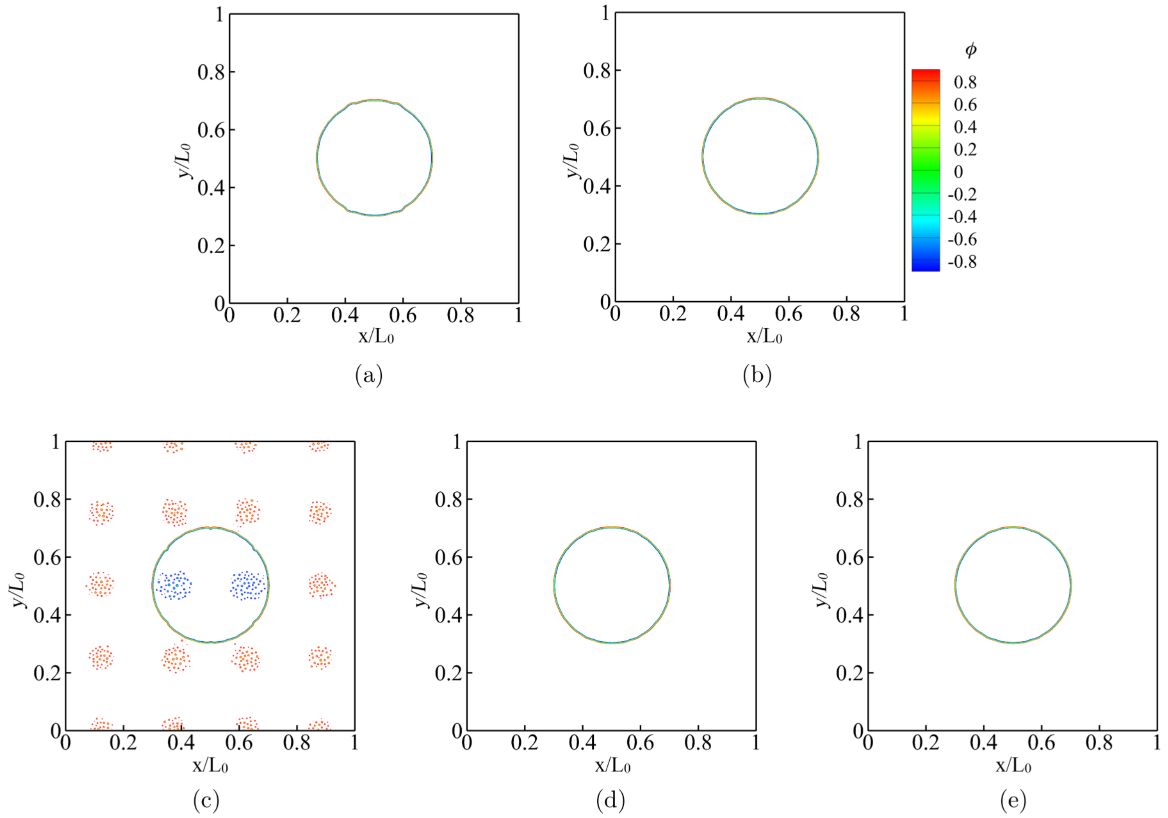

(a) (b)

(c) (d) (e)

FIG. 5. Comparisons of the interface shapes after two periods at $U = 0.25$ obtained by (a) MRT-A, (b) MRT-B, (c) MRT-C, (d) MRT-D, and (e) the present model. The contours are displayed within a range of $-0.9 \leqslant \phi \leqslant 0.9$.

point $(L/2, 0)$ are shown in Fig. 8(a). It can be seen that the density profiles for these four schemes match the analytical solution given by Eq. (65) very well. Figure 8(b) presents the pressure profiles at $y = 0$, where the pressure is defined by $P = p - \varepsilon_\phi^2 \phi \nabla^2 \phi - \varepsilon_\phi^2 |\nabla \phi|^2/2 + p_0$ and $p_0 = \phi \partial_\phi \psi - \psi$ is the equation of state [28]. According to the Laplace law, the pressure differences in two bulk phases should satisfy the relationship $\Delta P = P_h - P_l = \sigma / R$, where P_h and P_l are the pressure of heavy and light phases, respectively. The ratio between the surface tension calculated by the Laplace law and the analytical solution of Eq. (4), $\sigma_{\mathrm{LBM}}/\sigma$, is 0.9893, 0.9966, 0.9893, and 0.9966 for those four schemes, respectively. From this point of view, the mixed schemes are a little more accurate than the isotropic central schemes.

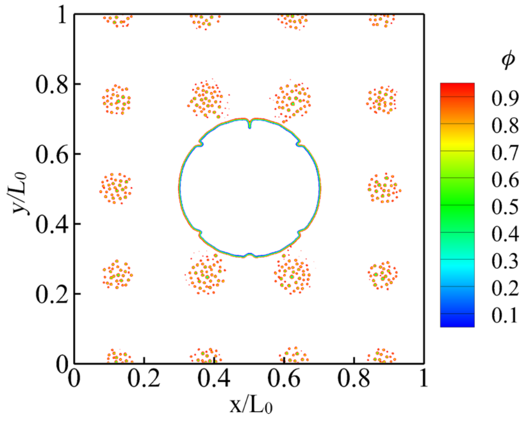

FIG. 6. Phase interface obtained by MRT-C by setting $\phi_h = 1$ and $\phi_l = 0$.

We also evaluate the mass conservation for the system and separated phases. The relative error for the total mass is defined as $E_t = |M_t(t) - M_t(0)|/M_t(0)$, where $M_t(t) = \sum_{\boldsymbol{x}} \rho(\boldsymbol{x}, t)$ is the total mass at time t. Similarly, we can obtain the mass for liquid phase $M_h(t)$ and vapor phase $M_l(t)$. Correspondingly, their relative changes are given by $E_h = [M_h(t) - M_h(0)]/M_t(0)$ and $E_l = [M_l(t) - M_l(0)]/M_t(0)$. Table IV lists the mass changes at equilibrium state. As pointed out in Ref. [49], the isotropic central scheme can keep the global mass conservation better than the mixed scheme. However, for the ACE-based lattice Boltzmann models, we did not find any obvious differences between these two schemes. Both schemes in MRT-B and the present model can conserve the global mass very well. As for the relative errors E_h and E_l, the results obtained by ACE-based models are two order of magnitude smaller than those in Ref. [49], which may benefit from the conservative nature of Allen-Cahn equation. Considering the performance on both reducing artificial currents and keeping mass conservation, the isotropic central forcing scheme should be a better choice for the present model and will be adopted in the following simulation.

B. Rayleigh-Taylor instability

We now examine the present model by the classic problem of Rayleigh-Taylor (RT) instability, which has been widely

TABLE IV. Relative mass changes of the total system and two separated phases at equilibrium state.

	E_h	E_l	E_t
Potential-ICS [49]	7.7815×10^{-2}	-7.7815×10^{-2}	7.4510×10^{-13}
Potential-MS [49]	-1.5485×10^{-2}	1.5483×10^{-2}	1.1805×10^{-6}
MRT-B-ICS	2.9848×10^{-4}	-2.9848×10^{-4}	-2.8972×10^{-12}
MRT-B-MS	3.2338×10^{-4}	-3.2338×10^{-4}	-2.7990×10^{-12}
Present-ICS	3.0045×10^{-4}	-3.0045×10^{-4}	-3.1161×10^{-12}
Present-MS	3.2451×10^{-4}	-3.2451×10^{-4}	-2.7969×10^{-12}

used to validate multiphase flow models [26,52–54]. Consider a rectangular domain of $[0, L_0] \times [-2L_0, 2L_0]$ filled with two layers of fluids with different densities. Initially, the denser fluid rests on the lighter one with a small perturbation $0.1L_0 \cos(2\pi x/L_0)$ on the interface $y = 0$. As the instability of interface develops, these two fluids will penetrate into each other. To be consistent with Ref. [26], the Atwood number $\mathrm{A}_t = \frac{\rho_h-\rho_l}{\rho_h+\rho_l}$ is introduced to describe the density rations between two phases. The reference velocity is chosen as $U_0 = \sqrt{gL_0}$. The timescale is specified as $t_0 = \sqrt{L_0/(gA_t)}$, such that the dimensionless time is $t^* = t/t_0$. In our simulations, a grid size of 200×800 is applied such that $L_0 = 200$. The interface width and the surface tension are $W = 5$ and $\sigma = 5 \times 10^{-5}$, respectively. Other parameters are set as $\mathrm{A}_t = 0.5$ ($\lambda_\rho = 3$), $\lambda_\mu = 1$, $\mathrm{Pe} = 1000$, and $\mathrm{Re} = 3000$. The nonslip boundary condition is applied on the top and bottom walls while the periodic boundary condition is imposed at the lateral sides.

The evolution of interface is shown in Fig. 9 at dimensionless time $t^* = 0.5$, 1, 1.5, 2, and 2.5. At the early stage, the falling spike of heavy fluid and rising bubble of light fluid are formed. With the decreasing of the height of spike tip, two counter-rotating vortices are appeared in the heavy fluid. The development of the roll-up structure of the present results agrees well with those in Refs. [32,55]. To quantitatively describe the temporal evolution of the interface, the positions of bubble and liquid front are treated as benchmark quantities. Fig. 10 plots the evolution of both bubble and liquid front obtained by the present model, along with the benchmark datas from previous studies [26,32,47]. Good agreements are reached among these results.

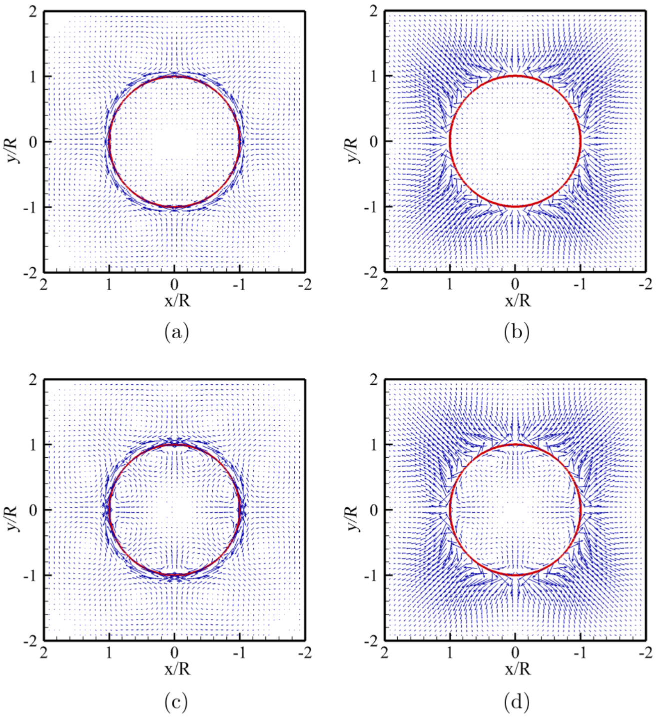

FIG. 7. Velocity fields at $t = 1 \times 10^6 \delta_t$: (a) MRT-B-ICS, (b) MRT-B-MS, (c) present-ICS, and (d) present-MS.

C. Single rising bubble

Bubble rising problems are investigated to test the accuracy of the present numerical schemes at high density ratios. A circular bubble with radius $r = 0.25$ m is initially placed at (0.5 m, 0.5 m) in the rectangular domain 1 m $\times$ 2 m. The scales for length and velocity are chosen as $L_0 = 2r$ and $U_0 = \sqrt{2gr}$, respectively. Table V lists dimensionless parameters which specify the test cases in our simulations. The corresponding physical parameters refer to Ref. [56]. For the present phase-field based LB model, the mesh 300×600 is adopted, which is fine enough to obtain grid-independent results. The bounce-back boundary condition is applied at the top and bottom boundaries, whereas the specular-reflection scheme is imposed on the lateral walls.

Simulations of case 1 are conducted at a relative low Eo number. In Fig. 11, the bubble shape at time $t = 3$ s is compared with the benchmark computations by FEM-based level-set method [56] and FEM-based phase-field method [57]. As it can be seen, the results by current method agree very well with both reference solutions. To describe the temporal evolution of a bubble quantitatively, the centroid of the bubble is introduced as benchmark quantity. The centroid movement plotted in Fig. 12 has a good agreement with the reference simulations.

For case 2, the density ratio and viscosity ratio are increased to 1000 and 100, respectively, and the Eo number is 125. In the scenario with high Eo, the surface tension force is relatively weaker and the bubble could undergo a severe shape

TABLE V. Dimensionless numbers for case 1 and case 2.

Case	λ_ρ	λ_μ	Re	Eo
1	10	10	35	10
2	1000	100	35	125

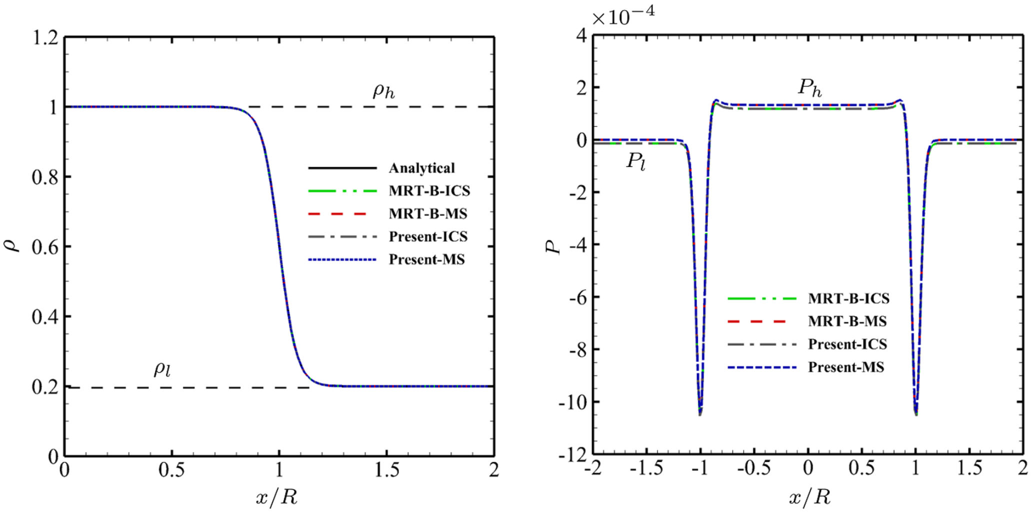

(a) (b)

FIG. 8. Static droplet tests simulated by MRT-B and the present modified model: (a) density profile and (b) pressure profile.

deformation. Typical time evolutions of the bubble shape are presented in Fig. 13. We compare the bubble shapes at time $t = 3$ s with the reference solutions in Fig. 14. Results obtained by the present model and FEM-based phase-field model are in a good agreement. Similar bubble shapes were also obtained by solving the flux-corrected Cahn-Hilliard equation in Ref. [27]. However, compared with the shapes obtained by the level-set model in Ref. [56], there exists some obvious discrepancies in bubble tails. These two tails did not break off and no satellite droplets were generated in the present model. This difference may be inherent to the phase-field approach, in which the interface is represented as a thin layer with finite width. As shown in Ref. [56], the size of the tails become very small before splitting. Therefore, the phase-field method will have trouble in capturing the filament structure as it is close to or smaller than the interface width. One can expect that the bubble may break off when the interface width tends to zero. The vertical movement of the bubble centroid, as shown in Fig. 15, is predicted very similarly for these three methods. And surprisingly, the different bubble tails have little effect on the bubble mass center. Although the benchmark solution for this case is rather inconclusive, we may still conclude that the

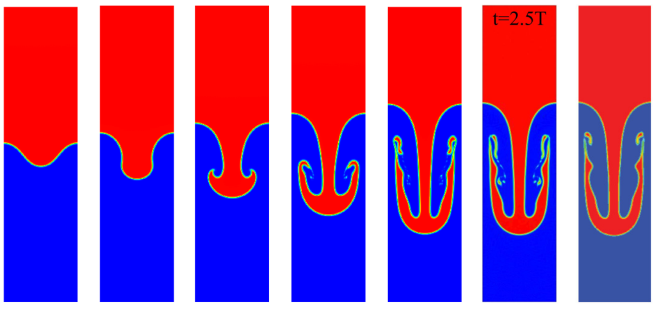

(a) (b) (c) (d) (e) (f) (g)

FIG. 9. Interface patterns of Rayleigh-Taylor instability: [(a)–(e)] The present model at $t^* = 0.5, 1, 1.5, 2, 2.5$; (f) Ref. [32] at $t^* = 2.5$; and (g) Ref. [55] at $t^* = 2.5$.

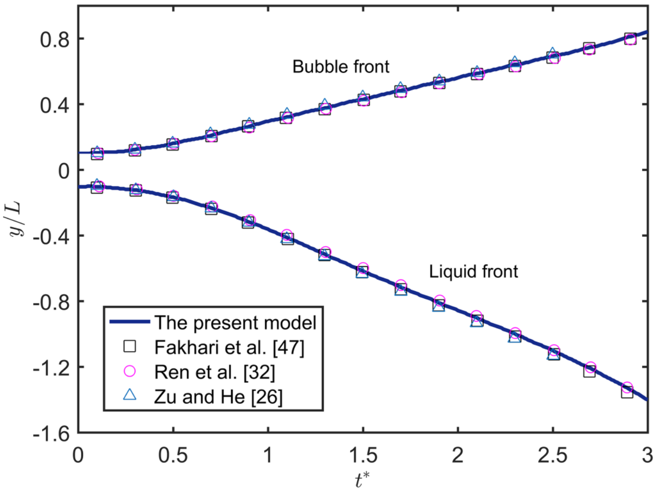

FIG. 10. Time evolution of the bubble front (upper curves) and liquid front (button curves).

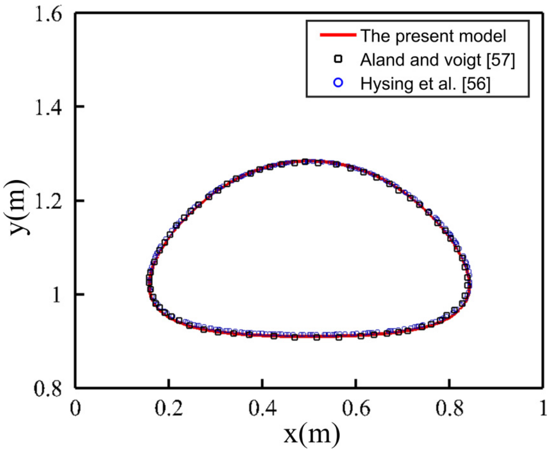

FIG. 11. Bubble shapes at the time $t = 3$ s for case 1, in comparison with benchmark computations conducted by Aland *et al.* [57] and Hysing *et al.* [56].

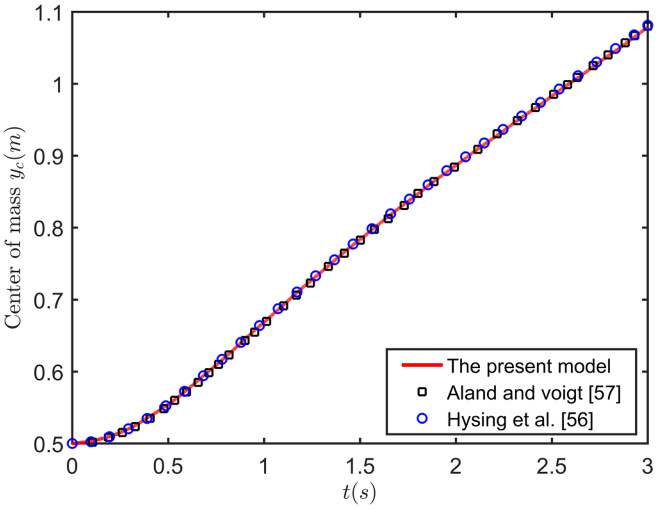

FIG. 12. Center of mass over time for case 1.

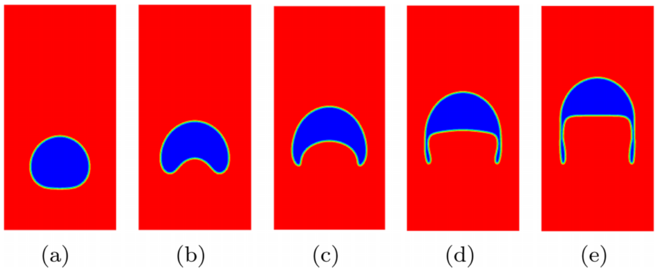

FIG. 13. Typical time evolution of the bubble interface for test case 2 with time interval $\Delta t = 0.6$ s.

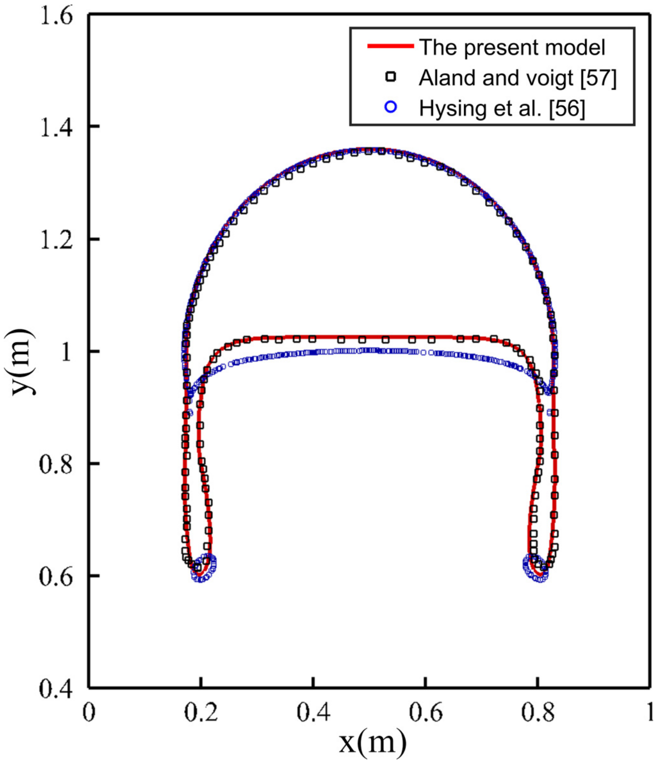

FIG. 14. Bubble shapes at the time $t = 3$ s for case 2, in comparison with benchmark computations [56,57].

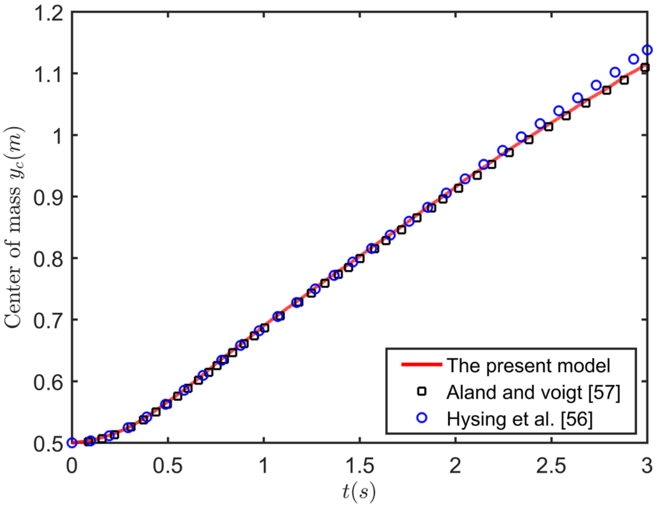

FIG. 15. Center of mass over time for case 2.

accuracy of the present model is comparable with FEM-based phase-field model.

V. SUMMARY AND CONCLUSION

We have proposed a modified multiple-relaxation-time lattice Boltzmann model for the conservative Allen-Cahn equation. By introducing an off-diagonal relaxation matrix, the target macroscopic equation can be recovered without introducing any extra terms. Free parameters in the equilibrium momentum vectors and relaxation matrix can be designed to improve the accuracy and stability. Combined with the pressure-based LB model for hydrodynamics, the proposed model can be applied to simulate the immiscible multiphase flow systems. Several numerical experiments have been conducted to demonstrate the accuracy and reliability of the present modified MRT-LB model. Results obtained by our model agree well with the corresponding analytical solutions or benchmark computations. Compared with conventional MRT-LB models without correction, the modified models have better performance under the conditions with relatively high Mach number. The computational cost for the present MRT-LB model is about 1% higher than MRT-A but almost the same with the modified model proposed by Ren *et al.* [32]. For the simulation of multiphase flows, the proposed MRT-LB model can easily handle the complex interface deformation, even in the case of high density and high viscosity ratios. The obtained results by the present LB model have comparable accuracy as the ones using FEM-based model. As a strategy to remove the artificial term in recovered macroscopic equation, the present model can be easily extended to treat the Cahn-Hlliard equation or other convection-diffusion equations.

ACKNOWLEDGMENTS

The authors are grateful to Dr. K. Luo for useful discussions. This work was financially supported by the National Science Fund for Distinguished Young Scholars (Grant No.

51625201), the National Key Research and Development Program of China (Grant No. 2016YFE0201600), the National Natural Science Foundation of China (Grant No. 51702066), the National Natural Science Foundation of China (Grant No. 51911530123), and the Key Project of the National Natural Science Foundation of China (Grant No. U1809210).

[1] M. Wörner, Microfluid. Nanofluid. **12**, 841 (2012).
[2] J. A. Sethian and P. Smereka, Annu. Rev. Fluid Mech. **35**, 341 (2003).
[3] D. Jacqmin, J. Comput. Phys. **155**, 96 (1999).
[4] I. Chakraborty, G. Biswas, and P. Ghoshdastidar, Int. J. Heat Mass Transf. **58**, 240 (2013).
[5] Y. Liu and X. Yu, J. Comput. Phys. **321**, 459 (2016).
[6] J. W. Cahn and J. E. Hilliard, J. Chem. Phys. **28**, 258 (1958).
[7] J. W. Cahn and J. E. Hilliard, J. Chem. Phys. **31**, 688 (1959).
[8] S. M. Allen and J. W. Cahn, Acta Metall. **27**, 1085 (1979).
[9] P. Yue, C. Zhou, and J. J. Feng, J. Comput. Phys. **223**, 1 (2007).
[10] Y. Li, J.-I. Choi, and J. Kim, Commun. Nonlin. Sci. Numer. Simul. **30**, 84 (2016).
[11] Y. Zhang and W. Ye, Commun. Comput. Phys. **22**, 422 (2017).
[12] Y. Sun and C. Beckermann, J. Comput. Phys. **220**, 626 (2007).
[13] E. Olsson and G. Kreiss, J. Comput. Phys. **210**, 225 (2005).
[14] P. H. Chiu and Y.-T. Lin, J. Comput. Phys. **230**, 185 (2011).
[15] X. Yang, J. J. Feng, C. Liu, and J. Shen, J. Comput. Phys. **218**, 417 (2006).
[16] A. Fakhari and M. H. Rahimian, Int. J. Mod. Phys. B **23**, 4907 (2009).
[17] A. K. Gunstensen, D. H. Rothman, S. Zaleski, and G. Zanetti, Phys. Rev. A **43**, 4320 (1991).
[18] X. Shan and H. Chen, Phys. Rev. E **47**, 1815 (1993).
[19] L. Chen, Q. Kang, Y. Mu, Y. L. He, and W. Q. Tao, Int. J. Heat Mass Transf. **76**, 210 (2014).
[20] Q. Li and K. H. Luo, Phys. Rev. E **88**, 053307 (2013).
[21] Y. Ba, H. Liu, Q. Li, Q. Kang, and J. Sun, Phys. Rev. E **94**, 023310 (2016).
[22] T. Inamuro, N. Konishi, and F. Ogino, Comput. Phys. Commun. **129**, 32 (2000).
[23] L. Luo, Phys. Rev. Lett. **81**, 1618 (1998).
[24] X. He, X. Shan, and G. D. Doolen, Phys. Rev. E **57**, R13(R) (1998).
[25] H. W. Zheng, C. Shu, and Y. T. Chew, Phys. Rev. E **72**, 056705 (2005).
[26] Y. Q. Zu and S. He, Phys. Rev. E **87**, 043301 (2013).
[27] C. Zhang, Z. Guo, and Y. Li, Int. J. Heat Mass Transf. **138**, 1128 (2019).
[28] H. Liang, B. C. Shi, Z. L. Guo, and Z. H. Chai, Phys. Rev. E **89**, 053320 (2014).
[29] A. Fakhari, M. Geier, and T. Lee, J. Comput. Phys. **315**, 434 (2016).
[30] H. L. Wang, Z. H. Chai, B. C. Shi, and H. Liang, Phys. Rev. E **94**, 033304 (2016).
[31] M. Geier, A. Fakhari, and T. Lee, Phys. Rev. E **91**, 063309 (2015).
[32] F. Ren, B. Song, M. C. Sukop, and H. Hu, Phys. Rev. E **94**, 023311 (2016).
[33] H. Huang, M. C. Sukop, and X. Lu, Multiphase Lattice Boltzmann Methods: Theory and Application (John Wiley & Sons, Ltd, 2015).
[34] Q. Li, K. H. Luo, Q. J. Kang, Y. L. He, Q. Chen, and Q. Liu, Prog. Energy Combust. Sci. **52**, 62 (2016).
[35] Z. Chai and T. S. Zhao, Phys. Rev. E **87**, 063309 (2013).
[36] Z. Chai, B. Shi, and Z. Guo, J. Sci. Comput. **69**, 355 (2016).
[37] C. Zhang, Z. Guo, and H. Liang, Phys. Rev. E **99**, 043310 (2019).
[38] A. Fakhari, D. Bolster, and L.-S. Luo, J. Comput. Phys. **341**, 22 (2017).
[39] A. Fakhari, M. Geier, and D. Bolster, Comput. Math. Appl. **78**, 1154 (2016).
[40] R. H. H. Abadi, M. H. Rahimian, and A. Fakhari, J. Comput. Phys. **374**, 668 (2018).
[41] R. Huang and H. Wu, J. Comput. Phys. **274**, 50 (2014).
[42] T. Biben, C. Misbah, A. Leyrat, and C. Verdier, Europhys. Lett. **63**, 623 (2003).
[43] R. Folch, J. Casademunt, A. Hernández-Machado, and L. Ramírez-Piscina, Phys. Rev. E **60**, 1724 (1999).
[44] H. Liang, J. Xu, J. Chen, H. Wang, Z. Chai, and B. Shi, Phys. Rev. E **97**, 033309 (2018).
[45] R. Huang and H. Wu, Phys. Rev. E **91**, 033302 (2015).
[46] T. Lee and C.-L. Lin, J. Comput. Phys. **206**, 16 (2005).
[47] A. Fakhari, T. Mitchell, C. Leonardi, and D. Bolster, Phys. Rev. E **96**, 053301 (2017).
[48] Z. L. Guo, C. G. Zheng, and B. C. Shi, Phys. Rev. E **83**, 036707 (2011).
[49] Q. Lou, Z. L. Guo, and B. C. Shi, Europhys. Lett. **99**, 64005 (2012).
[50] M. Gross, N. Moradi, G. Zikos, and F. Varnik, Phys. Rev. E **83**, 017701 (2011).
[51] D. D. Chiappini, G. G. Bella, S. S. Succi, F. F. Toschi, and S. S. Ubertini, Commun. Comput. Phys. **7**, 423 (2010).
[52] J. Yan, S. Li, A.-M. Zhang, X. Kan, and P.-N. Sun, J. Comput. Phys. **393**, 406 (2019).
[53] Y. Wang, C. Shu, H. Huang, and C. Teo, J. Comput. Phys. **280**, 404 (2015).
[54] J. J. Monaghan and A. Rafiee, Int. J. Numer. Methods Fluids **71**, 537 (2013).
[55] Q. Li, K. H. Luo, Y. J. Gao, and Y. L. He, Phys. Rev. E **85**, 026704 (2012).
[56] S.-R. Hysing, S. Turek, D. Kuzmin, N. Parolini, E. Burman, S. Ganesan, and L. Tobiska, Int. J. Numer. Methods Fluids **60**, 1259 (2009).
[57] S. Aland and A. Voigt, Int. J. Numer. Methods Fluids **69**, 747 (2012).